Proceedings of the ASME 2019
International Design Engineering Technical Conferences
and Computers and Information in Engineering Conference
IDETC/CIE2019
August 18-21, 2019, Anaheim, CA, USA

IDETC2019-97684

SIMULATION OF NUCLEATION AND GRAIN GROWTH IN SELECTIVE LASER MELTING OF TI-6AL-4V ALLOY

Dehao Liu and Yan Wang[1]
Woodruff School of Mechanical Engineering
Georgia Institute of Technology
Atlanta, GA 30332, USA

ABSTRACT

Selective laser melting (SLM) builds parts by selectively melting metallic powders layer by layer with a high-energy laser beam. It has a variety of applications in aerospace, medical device, and other low-volume manufacturing. Nevertheless, the lack of fundamental understanding of the process-structure-property (P-S-P) relationship for better quality control inhibits wider applications of SLM. Recently, a mesoscale simulation approach, called phase-field and thermal lattice Boltzmann method (PF-TLBM), was developed to simulate microstructure evolution of alloys in SLM melt pool with simultaneous consideration of solute transport, heat transfer, phase transition, and latent heat effect. In this paper, a nucleation model is introduced in the PF-TLBM model to simulate heterogeneous nucleation at the boundary of melt pool in SLM. A new method is also developed to estimate the thermal flux out of the SLM melt pool model given a constant cooling rate. The effects of latent heat and cooling rate on dendritic morphology and solute distribution are studied. The simulation results of Ti-6Al-4V alloy suggest that the inclusion of latent heat is necessary because it reveals the details of the formation of secondary arms, reduces overestimated microsegregation, and provides more accurate kinetics of dendritic growth.

Keywords: selective laser melting; nucleation; dendritic growth; phase-field method; thermal lattice Boltzmann method

1. INTRODUCTION

As a powder bed based additive manufacturing (AM) technique, selective laser melting (SLM) builds three-dimensional (3D) parts by melting layers of fine-grained metallic powders with a laser beam. It significantly improves the manufacturability of complex geometries and heterogeneous materials. SLM has the potential to be widely applied in various industries including automotive, aerospace, biomedical, energy, and other high-value low-volume manufacturing environments. However, the lack of fundamental understanding of process-structure-property (P-S-P) relationship of SLM becomes the bottleneck to produce defect-free, structurally sound, and reliable AM parts. There is a critical need to understand the rapid solidification process during which microstructures are formed and the properties of solid parts are determined.

During the complex process of solidification, interactions between solute transport, heat transfer, and phase transition have significant effects on the formation of the microstructure. The final solidified microstructure determines the mechanical strength, thermal conductivity, corrosion resistance, and other properties of the AM parts. A thorough understanding of the rapid solidification process allows us to establish the P-S-P relationship for process design and optimization. Establishing the P-S-P relationship in high-dimensional parameter space requires a large number of samples. Currently the capabilities of in-situ observation for rapid solidification at nano- and micro-scales are very limited. Compared to experimental studies, simulation is more cost-effective to reveal the cause-effect relations. Multiscale multi-physics simulation sometime becomes the only viable approach to study complex phenomena.

Various models have been developed to understand and predict microstructure evolution during solidification. These include front-tracking, enthalpy, level-set, cellular automaton (CA), and phase-field method (PFM) [1]. Particularly, PFM and CA are the most used methods. CA is computationally much more efficient than PFM so that it can be applied to simulate large systems. However, PFM [2,3] can reveal more details of dendritic growth dynamics and side branch emission. CA predictions of anisotropic gain structures are sensitive to the choice of mesh shapes. The dendrite tip velocities predicted by

[1] Contact author: yan.wang@me.gatech.edu

PFM agree with the Lipton-Glicksman-Kurz model more than CA results [4].

PFM has been widely used to simulate dendritic growth in the processes of casting, welding, and SLM. The rapid solidification in SLM is a highly complex process where it is not appropriate to make equilibrium assumptions of thermal field and melt flow. A multi-physics simulation approach is necessary to understand the interactions among temperature, velocity, and phase fields. Limited work has been done in multi-physics PFM for SLM simulation. In the study of Keller et al. [5], finite element analysis (FEA) was employed to obtain the geometric feature and the thermal history of the laser melt pool, which were used in the subsequent PFM simulation of dendritic growth of IN625 alloy. The predicted primary arm spacings agreed with the experimentally measured spacings, whereas the prediction of microsegregation was less intensive than that by DICTRA simulations. Wang and Chou [6] combined finite element thermal model and PFM to investigate the effects of build height and scanning speed on the dendritic growth of IN718 alloy in SLM. In the work of Acharya et al. [7], computational fluid dynamics (CFD) analysis was utilized to predict the melt pool shape, and PFM was used to simulate dendritic growth of IN718 alloy in SLM. The dendritic morphology and microsegregation were validated with experimental results. Liu and Wang [8,9] developed a phase-field and thermal lattice Boltzmann method (PF-TLBM) to investigate the effects of latent heat and forced melt flow on the dendritic morphology, concentration, and temperature field during SLM process. The simulation results of Ti-6Al-4V showed that the consideration of latent heat is necessary because it reveals the details of the formation of secondary arms and provides more realistic kinetics of dendritic growth. The predicted secondary arm spacing was verified with the analytical calculation.

In this work, the PF-TLBM is extended to include a nucleation model for heterogeneous nucleation and dendritic growth. Nucleation affects the accuracy of simulated microstructures in SLM, but it has only been considered in few studies of PFM simulation. Shimono et al. [10] simulated the columnar-to-equiaxed transition of Ti-6Al-4V alloy during the AM process by coupling PFM with the calculation of phase diagrams (CALPHAD). A continuous Gaussian nucleation distribution was used to describe the grain density increase with the increase in undercooling. The empirical nucleation parameters, such as maximum nucleation density and mean undercooling, were adjusted to reach the agreement between simulations and experiments. However, this empirical model missed some important physics of nucleation compared to classical nucleation theory (CNT). Gránásy et al. [11,12] described two methods to include homogeneous nucleation into PFM simulations. The first method was introducing Langevin noise terms in PFM to force nucleation, whereas the second one was to calculate the nucleation energy barrier using PFM and place nuclei based on a constant cooling rate. The nucleation energy barrier was determined by solving the Euler–Lagrange equations of the phase field and composition field. PFM was also used to determine the nucleation energy barrier for heterogeneous nucleation, where appropriate boundary conditions were introduced at the foreign wall to realize the required contact angle [13]. Pusztai et al. [14] introduced Langevin noise terms in PFM to simulate homogeneous and heterogeneous nucleation in polycrystalline. However, by introducing Langevin noises, nucleation could occur at anywhere in the simulation domain rather than the solid-liquid interface because of the nature of stochastic partial differential equation. The model works well for large melt pools such as in casting, but not accurate in SLM with small melt pools. In powder based SLM, the size of melt pool is usually less than 100 μm. Furthermore, it is known that nucleation and growth occur on different time scales, the observation of nucleation would require an impractically large number of integration cycles to sample frequently enough. Therefore, Simmons et al. [15] replaced the Langevin noise terms in PFM with a Poisson seeding algorithm, where viable nuclei were introduced at a time-dependent nucleation rate. However, the developed model is used for homogeneous nucleation rather than heterogeneous nucleation. In the work of Li et al. [16], the nucleation kinetics of binary melts is calculated based on CNT. The model was originally used to simulate polycrystalline solidification of NiCu alloy in casting, where the clear columnar-to-equiaxed transition (CET) was clearly shown. However, in this work, the heterogenous nucleation occurred in the melt pool rather than the boundary of the melt pool, which cannot reflect the actual solidification process in SLM. In SLM, heterogeneous nucleation tends to occur at the solid-liquid interface at the bottom of the small melt pool as experimentally observed.

In this study, a nucleation model is introduced into the PF-TLBM framework for simulating microstructure evolution in SLM. The main contribution of this work is the simulation of nucleation and dendritic growth of Ti-6Al-4V alloy in the small melt pool of SLM, where heterogeneous nucleation tends to occur at the boundary. A method to approximate the thermal flux out of the small melt pool for PF-TLBM is also developed, given a constant cooling rate.

In the remainder of this paper, the formulation of PF-TLBM and the new nucleation model are described in Section 2. The simulation settings of SLM melt pool, simulation results of Ti-6Al-4V alloy, and the effects of latent heat and cooling rate on dendritic growth are shown in Section 3. The quantitative analyses of thermal history, time evolution of solid phase fraction, and composition distribution are also provided.

2. METHODOLOGY

In this section, the formulation of PF-TLBM is briefly described. The PFM formulation is introduced in Section 2.1. The thermal lattice Boltzmann method (TLBM) is introduced in Section 2.2. More details about PF-TLBM can be found in Ref. [7]. The phase field and composition are calculated by solving the Allen-Cahn equation and diffusion equation. The temperature field and velocity field are obtained from TLBM. PFM and TLBM are tightly coupled by updating and exchanging the information of phase, composition, and temperature fields in each iteration of simulation. In Section 2.3, the new nucleation

model is described, which is used to simulate the heterogeneous nucleation in the mushy zone of melt pool in the SLM process.

2.1 Phase-field method

The multi-phase field method is used to describe the liquid-solid phase transition during the solidification process. The main advantage of PFM is that the movement of the interface of the microstructure is tracked implicitly rather than explicitly. In PFM, a continuous variable named phase field, ϕ, is used to keep track of the solid phase fraction in the simulated domain. The microstructure evolution is modeled by the time evolution of the phase field.

The kinetic equation for the phase field is given by

$$\frac{\partial \phi}{\partial t} = M_\phi \begin{Bmatrix} \sigma^*(\mathbf{n})\left[\nabla^2\phi + \frac{\pi^2}{\eta^2}\left(\phi - \frac{1}{2}\right)\right] \\ + \frac{\pi}{\eta}\sqrt{\phi(1-\phi)}\Delta G_V \end{Bmatrix}, \quad (1)$$

where M_ϕ is the effective interface mobility, η is the interface width, and $\mathbf{n} = \nabla\phi/|\nabla\phi| = (n_x, n_y)$ is the local normal direction of the interface. The anisotropic interface energy stiffness is defined as

$$\sigma^* = \sigma + \frac{\partial^2\sigma}{\partial\psi^2} = \sigma_0^*\left[1 - 3\delta + 4\delta\left(n_x^4 + n_y^4\right)\right], \quad (2)$$

where σ is the interface energy, $\psi = \arctan(n_y/n_x)$ indicates the grain orientation, σ_0^* is the prefactor of interface energy stiffness, and δ is the anisotropy strength of interface energy stiffness. The driving force is described by

$$\Delta G_V = \Delta S(T_m - T + m_l C_l), \quad (3)$$

where ΔS represents the entropy difference between solid and liquid phases, T_m represents the melting temperature of a pure material, T represents the temperature, m_l represents the liquidus slope, and C_l represents the weight percentage (wt%) of solute in the liquid phase.

The kinetic equation for the composition field is given by

$$\frac{\partial C}{\partial t} = \nabla\cdot[D_l(1-\phi)\nabla C_l] + \nabla\cdot\mathbf{j}_{at}, \quad (4)$$

where $C = \phi C_s + (1-\phi)C_l$ is the overall composition of a solute in the simulation domain and C_s is the composition of the solid phase. During rapid solidification, the dynamic partition coefficient can be calculated according to Aziz's model [17]

$$k = \frac{C_s}{C_l} = \frac{k_e + V_I\lambda/D_l}{1 + V_I\lambda/D_l}, \quad (5)$$

where k_e is the equilibrium partition coefficient, λ is the actual width of the interface in atomic dimensions, and V_I is the interface velocity. The diffusion coefficient of the liquid phase is given by

$$D_l = D_0\exp\left(\frac{-\Delta E}{RT}\right), \quad (6)$$

where D_0 is the prefactor of diffusion coefficient of liquid phase, ΔE is activation energy, and R is gas constant. The anti-trapping current is introduced and defined as

$$\mathbf{j}_{at} = \frac{\eta}{\pi}\sqrt{\phi(1-\phi)}(C_l - C_s)\frac{\partial\phi}{\partial t}\frac{\nabla\phi}{|\nabla\phi|}, \quad (7)$$

which is used to remove the unphysical solute trapping caused by the finite interface width.

2.2 Thermal lattice Boltzmann method

In this work, the melt is assumed to be static in the small pool for simplification. The effect of Marangoni flow on dendritic growth will be considered in future work. TLBM is used to calculate temperature field only in this study.

The conservation equation of energy is given by

$$\frac{\partial T}{\partial t} = \nabla\cdot(\alpha\nabla T) + \dot{q}, \quad (8)$$

where α is the thermal diffusivity. The released latent heat during solidification is given by

$$\dot{q} = \frac{L_H}{c_p}\frac{\partial\phi}{\partial t}, \quad (9)$$

where L_H is the latent heat of fusion, and c_p is the specific heat capacity. Instead of solving the conservation equation directly, a particle distribution function of temperature $g_i(\mathbf{x}, t)$ is utilized to capture the dynamics of the system in TLBM. Particles move dynamically between neighboring discretized lattice nodes in TLBM. In a two-dimensional D2Q9 scheme, each node has eight neighbors. The velocity vector along the *i*-th direction in the lattice with respect to a reference node is given by

$$\mathbf{e}_i = \begin{cases} (0,0), & i = 0 \\ (\pm c, 0), (0, \pm c), & i = 1, \cdots, 4, \\ (\pm c, \pm c), & i = 5, \cdots, 8 \end{cases} \quad (10)$$

where $c = \Delta x/\Delta t$ is the lattice velocity with grid spacing Δx and time step Δt, and index *i* corresponds to a unique direction in the lattice. The kinetic equation of particle distribution of temperature is given by

$$g_i(\mathbf{x} + \mathbf{e}_i\Delta t, t + \Delta t) = \frac{1}{\tau_g}\left[g_i^{eq}(\mathbf{x}, t) - g_i(\mathbf{x}, t)\right] + Q_i(\mathbf{x}, t)\Delta t, \quad (11)$$

where $\tau_g = 3\alpha/(c^2\Delta t) + 0.5$ is the dimensionless relaxation time, $g_i^{eq}(\mathbf{x}, t) = \omega_i T$ is the equilibrium distribution, and

$$Q_i = \left(1 - \frac{1}{2\tau_g}\right)\omega_i\dot{q} \quad (12)$$

is the heat source term. In D2Q9 scheme, the weights ω_i 's associated with direction *i*'s are

$$\omega_i = \begin{cases} 4/9, & i = 0 \\ 1/9, & i = 1, \cdots, 4 \\ 1/36, & i = 5, \cdots, 8 \end{cases}. \quad (13)$$

During each iteration, the temperature T can be calculated from the particle distribution of temperature g_i's as

$$T = \sum_i g_i + \frac{\Delta t}{2}\dot{q}. \quad (14)$$

In the SLM process, heat transfer is much faster than solute diffusion because thermal diffusivity can be three orders of magnitude larger than solute diffusivity. In order to improve the computational efficiency, a fine grid spacing dx is used for the PFM simulation, whereas a coarse grid spacing $\Delta x = 50\,dx$ is used for the TLBM simulation. The same time step Δt is used

for both simulations. The results of TLBM are linearly interpolated as the input for the PFM model, whereas the results of PFM are averaged and transferred to the TLBM model in each iteration. The anti-bounceback scheme is used for the thermal boundary condition. The particle distribution of temperature at the boundary node $g_{\bar{\imath}}(\mathbf{x}_b, t+\Delta t)$, for direction $\bar{\imath}$ such that $\mathbf{e}_{\bar{\imath}} = -\mathbf{e}_i$, is determined by

$$g_{\bar{\imath}}(\mathbf{x}_b, t+\Delta t) = -g_i(\mathbf{x}, t) - \frac{1}{\tau_g}\left[g_i^{eq}(\mathbf{x}, t) - g_i(\mathbf{x}, t)\right] + 2\omega_i T_w. \quad (15)$$

The temperature of the wall T_w is given by

$$T_w = T_b - \frac{q_H \Delta x}{2\kappa}, \quad (16)$$

where T_b is the temperature at the boundary node, q_H is the outward heat flux at the boundary, and κ is the thermal conductivity of the material.

2.3 Nucleation model

During the SLM process, columnar dendrites grow from the bottom of melt pool upwards, as usually observed in experiments. Therefore, it is reasonable to assume that heterogeneous nucleation dominates, which also has a much lower energy barrier than homogeneous nucleation. To simulate the heterogeneous nucleation process, a Poisson seeding algorithm [15,16] is adopted. Nucleation can be treated as fully localized events and can be modeled as a Poisson process. The major assumption is the spatial and temporal independence between events with the memoryless property. The nucleation probability is given by

$$P_n = 1 - exp(-Iv\Delta t), \quad (17)$$

where I is the nucleation rate, v is the cell spacing, and Δt is a sufficiently small time interval. Based on the CNT, the nucleation rate can be calculated by

$$I = I_0 exp\left[-\frac{16\pi\sigma^3 f(\bar{\theta})}{3kT(\Delta G_V)^2}\right], \quad (18)$$

where $I_0 \approx 5 \times 10^{15}\ \mathrm{m}^2/\mathrm{s}$ is the prefactor of the nucleation rate determined by the jump frequency across the interface, σ is the interface energy, $f(\bar{\theta}) = (2 - 3cos\bar{\theta} + cos^3\bar{\theta})/4 = 1 \times 10^{-5}$ with $\bar{\theta}$ as the contact angle, k is the Boltzmann constant, ΔG_V is the driving force in the Eq. (3). The prefactor of the nucleation rate is calibrated based on the average β grain size of Ti-6Al-4V alloy in the SLM experiment [18], which is 30 μm. During each time step, the nucleation probability P_n is calculated at each liquid cell at the boundary of the melt pool during the simulation. At the same time, a uniform random variable will be generated and compared with the nucleation probability P_n. If the random variable is less than the nucleation probability P_n, then the nucleus is planted.

3. RESULTS AND DISCUSSION

This section describes the simulation setup, and the simulation results which show the effects of latent heat and cooling rate on dendritic growth of Ti-6Al-4V alloy in the melt pool in SLM. The quantitative analyses of thermal history, time evolution of solid phase fraction, and composition distribution are also provided.

3.1 Computational setup

The PF-TLBM framework is used to simulate nucleation and dendritic growth of Ti-6Al-4V alloy in the melt pool during the SLM process. By using the pseudo-binary approach, the ternary Ti-6Al-4V alloy is treated as a binary alloy, and the solute is the combination of Al and V. The physical properties of Ti-6Al-4V alloy are listed in TABLE 1 [9]. The algorithm is implemented in C++ programming language and integrated with an open source software called OpenPhase [19]. PFM and lattice Boltzmann method (LBM) have been implemented in the original OpenPhase. There are three main contributions of our work. First, LBM has been extended as TLBM in OpenPhase so that heat transfer can be simulated. Second, a probabilistic nucleation model has been introduced in the framework. Finally, a double-mesh scheme has been implemented to improve computational efficiency.

TABLE 1: Physical properties of Ti-6Al-4V alloy

Physical properties	Value
Melting point of pure Ti, T_m [K]	1941
Liquidus temperature, T_l [K]	1928
Solidus temperature, T_s [K]	1878
Liquidus slope, m_l [K/wt%]	-1.3
Equilibrium partition coefficient, k_e	0.206
Prefactor of interface energy stiffness, σ_0^* [J/m^2]	0.26
Interfacial energy stiffness anisotropy, δ	0.35
Interface mobility, M_ϕ [m^4/(J·s)]	2×10^{-8}
Entropy difference, ΔS [J/(m^3·K)]	-6×10^{5}
Physical interface width, λ [m]	3×10^{-9}
Prefactor of diffusion coefficient of liquid phase, D_0 [m^2/s]	0.059
Activation energy, ΔE [J/mol]	2.5×10^{5}
Kinematic viscosity, ν [m^2/s]	6.11×10^{-7}
Thermal diffusivity, α [m^2/s]	8.1×10^{-6}
Thermal conductivity, κ [W/(m·K)]	28
Latent heat of fusion, L_H [J/kg]	2.90×10^{5}
Specific heat capacity, c_p [J/(kg·K)]	872
Density, ρ [kg/m^3]	4000
Heat transfer coefficient, h [W/(m^2·K)]	50
Emissivity, ε	0.5

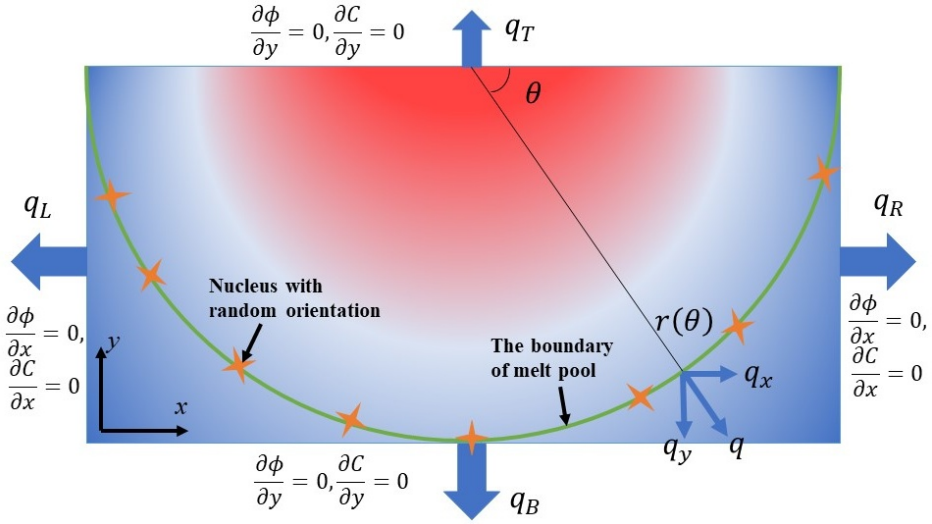

FIGURE 1: Setup of boundary conditions.

Since thermal diffusivity is three orders of magnitude larger than solute diffusivity, a double-mesh scheme is adopted in all simulations to reduce computational cost. A fine grid spacing $dx = 0.2$ μm is used for the PFM simulation, whereas a coarse grid spacing $\Delta x = 50\,dx = 10$ μm is used for the TLBM simulation. Based on the stability analysis, the upper limit of the time step should be $\Delta t \le min\{dx^2/(4D_l), \Delta x^2/(4\nu), \Delta x^2/(4\alpha)\}$. As a result, the time step $\Delta t = 0.2$ μs is applied in all simulation runs. During the SLM process, the size of the melt pool is determined by hatching spacing, layer thickness, laser power and other factors. The common hatching spacing is 100 μm and the usual layer thickness is 50 μm. Consequently, the length of the simulated two-dimensional domain is $L_x = 500\,dx = 100$ μm in the x-direction and the width is $L_y = 250\,dx = 50$ μm in the y-direction. The interface width is $\eta = 5\,dx$, meaning that there are 6 nodes on the interface or boundary layer. The initial composition of the solute is set as $C_0 = 10$ wt% for the whole simulation domain.

The setup of boundary conditions for all simulations is schematically illustrated in FIGURE 1. The rectangular region stands for the cross section of the melt pool, which is perpendicular to the scanning direction. The semicircular curve indicates the boundary of melt pool, where nuclei with random distributions are generated. Zero Neumann conditions are set at the all boundaries for the phase field ϕ and composition C. Four constant heat fluxes q_T, q_B, q_L, and q_R are applied at the top, bottom, left, and right boundaries, respectively. They are estimated based on their geometric relation to the heat flux $\mathbf{q}$ which is normal to the boundary of melt pool. More specifically, $\mathbf{q}$ is decomposed into three heat fluxes q_B, q_L, and q_R. It is assumed that the heat flux $\mathbf{q}$ has a constant magnitude. It is necessary to determine the relationship between heat fluxes q_B, q_L, and q_R so that the magnitude of heat fluxes at boundaries can be calculated. To make it more general, it is assumed that the shape of the melt pool is a semi-ellipse, which is defined as

$$r(\theta) = (acos\theta, bsin\theta), \tag{19}$$

where a is the major axis, b is the minor axis, and θ is an angular parameter that defines the position. The heat flux $\mathbf{q}$ normal to the boundary of the melt pool has a constant magnitude and is given by

$$\mathbf{q} = q\mathbf{N} = \frac{q}{\sqrt{a^2sin^2\theta + b^2cos^2\theta}}(bcos\theta, asin\theta), \tag{20}$$

where $\mathbf{N}$ is the unit normal vector perpendicular to the boundary of the melt pool. It is obvious that the heat flux $\mathbf{q}$ can be decomposed to $\mathbf{q_x} = q/\sqrt{a^2sin^2\theta + b^2cos^2\theta}(bcos\theta, 0)$ and $\mathbf{q_y} = q/\sqrt{a^2sin^2\theta + b^2cos^2\theta}(0, asin\theta)$. Because the semi-ellipse is symmetric with respect to the y-axis, let us consider the case when $-2/\pi \le \theta \le 0$ first. By using vector calculus, the rate of heat flow caused by the horizontal heat flux $\mathbf{q_x}$ can be calculated by

$$\begin{aligned}\dot{Q}_x &= \int_{-\frac{\pi}{2}}^{0} \mathbf{q_x}\cdot\mathbf{N}\,ds \\ &= \int_{-\frac{\pi}{2}}^{0} \mathbf{q_x}\cdot\mathbf{N}\,|r'(\theta)|d\theta \\ &= \int_{-\frac{\pi}{2}}^{0} \frac{qb^2cos^2\theta}{\sqrt{a^2sin^2\theta+b^2cos^2\theta}}d\theta.\end{aligned} \tag{21}$$

Similarly, the rate of heat flow caused by the vertical heat flux $\mathbf{q_y}$ is given by

$$\begin{aligned}\dot{Q}_y &= \int_{-\frac{\pi}{2}}^{0} \mathbf{q_y}\cdot\mathbf{N}\,ds \\ &= \int_{-\frac{\pi}{2}}^{0} \mathbf{q_y}\cdot\mathbf{N}\,|r'(\theta)|d\theta \\ &= \int_{-\frac{\pi}{2}}^{0} \frac{qa^2sin^2\theta}{\sqrt{a^2sin^2\theta+b^2cos^2\theta}}d\theta.\end{aligned} \tag{22}$$

Both $\dot{Q}_x$ and $\dot{Q}_y$ can be calculated by numerical integration. On the other hand, from the definition of rate of heat flow, we have

$$\frac{\dot{Q}_x}{\dot{Q}_y} = \frac{q_B L_x}{2 q_R L_y}. \quad (23)$$

Because of the symmetry of the melt pool, the rates of heat flow at the left and right boundaries are the same, as

$$q_L L_y = q_R L_y. \quad (24)$$

As a simplified version, the boundary of the melt pool in this paper is semicircular. The rates of heat flow along the x-direction and y-direction are the same, as

$$\frac{\dot{Q}_x}{\dot{Q}_y} = \frac{q_B L_x}{2 q_R L_y} = 1. \quad (25)$$

Based on Eqs. (23)-(25), we have

$$q_B L_x = 2 q_L L_y = 2 q_R L_y. \quad (26)$$

The heat flux at the top boundary caused by the convection and radiation heat transfer is defined as

$$q_T = h(T_l - T_0) + \sigma_{SB} \varepsilon (T_l^4 - T_0^4) \quad (27)$$

where σ_{SB} is Stefan–Boltzmann constant and $T_0 = 298$ K is the room temperature. Given a constant cooling rate $\dot{T}$, the other three heat fluxes q_B, q_L, and q_R can be calculated based on the energy balance equation

$$L_x L_y \rho c_p \dot{T} = q_T L_x + q_B L_x + q_L L_y + q_R L_y. \quad (28)$$

After four heat fluxes are obtained, the temperature of the wall T_w can be updated in each iteration based on Eq. (16).

(a) Phase field at 0.8 ms

(b) Phase field at 1.6 ms

(c) Phase field at 2.4 ms

(d) Phase field at 3.2 ms

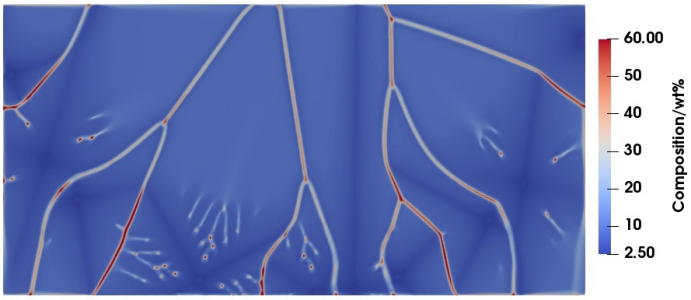

(e) Composition field at 3.2 ms

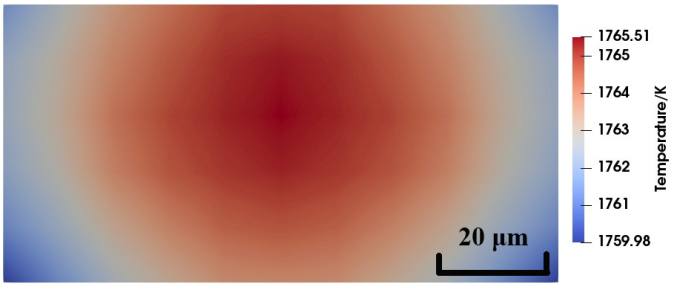

(f) Temperature field at 3.2 ms

FIGURE 2: Dendritic growth without latent heat when $\dot{T} = 2 \times 10^4$ K/s.

3.2 Dendritic growth without latent heat

The dendritic growth of Ti-6Al-4V alloy is first simulated without the release of latent heat for comparison. A constant cooling rate $\dot{T} = 2 \times 10^4$ K/s is used. The simulation results are shown in FIGURE 2. The grain identification (ID) 0 represents the liquid phase, whereas other grain IDs represent solid phases with different orientations. During the rapid solidification process, the columnar dendritic growth dominates in the melt pool, as shown in FIGURE 2.

At the time of 0.8 ms, the columnar dendritic growth pattern is observed, as shown in FIGURE 2(a). The primary arms and secondary arms still can be differentiated. As a result of the anisotropy of interface energy, the primary arms grow faster than secondary arms. Since the release of latent heat is ignored, the secondary arms grow so fast that they quickly merge with each other as shown in FIGURE 2(b). At the time of 3.2 ms, the melt has been completely solidified as shown in FIGURE 2(d). The composition field at 3.2 ms is shown in FIGURE 2(e), where primary arms and secondary arms can be differentiated easily. The microsegregation occurs at the grain boundaries and the small pockets between secondary arms. In FIGURE 2(f), the temperature at the upper center of the melt pool is the highest, which is caused by the setup of heat fluxes at the boundaries. Since the primary arms aligned with the temperature gradient grow faster than those do not, this results in the radial distribution pattern of columnar dendrites in the melt pool, as shown in FIGURE 2(d).

(a) Phase field at 0.8 ms

(b) Phase field at 1.6 ms

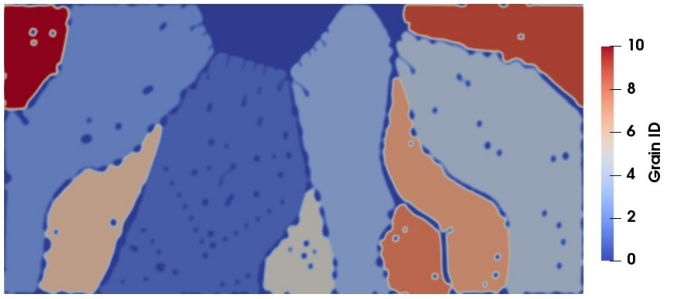

(c) Phase field at 2.4 ms

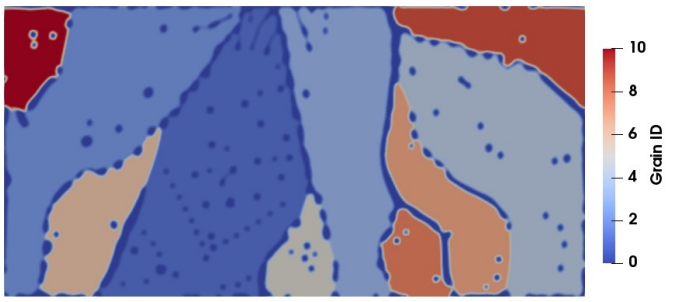

(d) Phase field at 3.2 ms

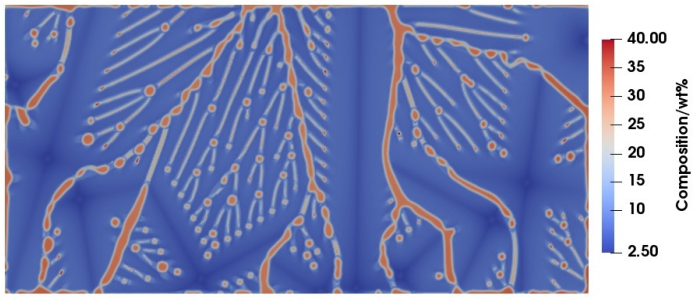

(e) Composition field at 3.2 ms

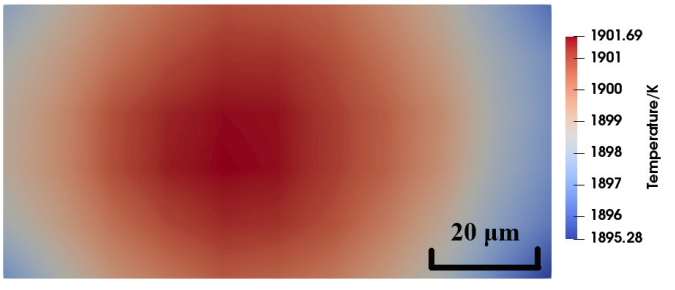

(f) Temperature field at 3.2 ms

FIGURE 3: Dendritic growth with latent heat when $\dot{T} = 2 \times 10^4$ K/s.

3.3 Dendritic growth with latent heat

In the second case, the dendritic growth with the release of latent heat is simulated. The cooling rate $\dot{T} = 2 \times 10^4$ K/s keeps the same. FIGURE 3 shows the simulation results. At the time of 0.8 ms, a clear dendritic growth pattern is shown in FIGURE 3(a), where primary arms and secondary arms can be differentiated easily. When the dendrites continue to grow, partial secondary arms merge with each other as shown in FIGURE 3(b-d). However, there is still some residual melt between grains. The melt is not completely solidified even at the time of 3.2 ms, as shown in FIGURE 3(d). The composition field at 3.2 ms is shown in FIGURE 3(e), where secondary arms can still be observed clearly. The small pocket of the liquid phase at grain boundaries may remain liquid for a long period of time until solid diffusion takes away the remaining solute supersaturation before it is completely solidified. The microsegregation at grain boundaries in the case with latent heat is lower than that in the case without latent heat. FIGURE 3(f) shows the temperature field at 3.2 ms. The temperature in the case with latent heat is higher than that in the case without latent heat. The maximum temperature is higher than the temperature of liquidus, which accounts for the fact that the melt is not completely solidified. Based on the above comparison, the inclusion of latent heat is necessary because it reveals the details of the formation of secondary arms.

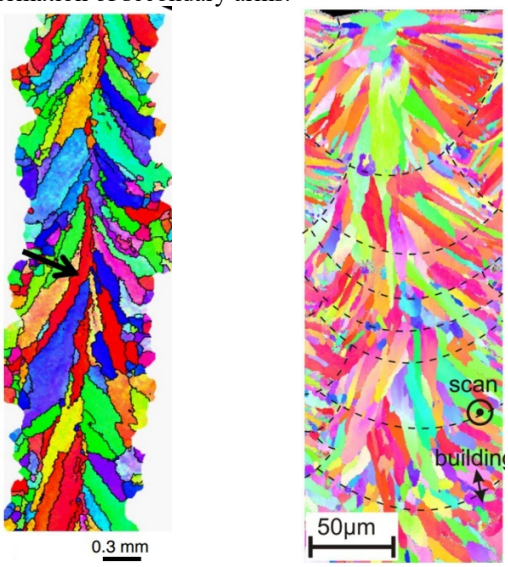

(a) (b)

FIGURE 4: Experimental EBSD result of the cross section of the sample. (a) Reconstructed β grain structure of Ti-6Al-4V alloy produced by electron beam selective melting (EBSM) (Courtesy of Antonysamy et al. [20]); (b) Grain structure of AlSi10Mg sample produced by SLM (Courtesy of Thijs et al. [21]).

The simulated grain structure in FIGURE 3(d) qualitatively matches with the experimental observation by electron backscatter diffraction (EBSD) [20,21] in FIGURE 4. After one laser or electron beam pass, the dendrites at the curved boundary of the melt pool will grow and result in a radial distribution pattern. Besides, the secondary arm spacing of the simulated dendrite is $\lambda_2 = 2.8$ μm, which is close to the calculated value $\lambda_2 = 3.7$ μm based on the analytical model developed by Bouchard and Kirkaldy [22], as

$$\lambda_2 = 12\pi \left[\frac{4\sigma D_l^2}{C_0(1-k)^2 \rho L_H V_l^2}\right]^{\frac{1}{3}}. \quad (29)$$

The difference between the predicted and observed secondary arm spacing could be caused by parameter uncertainty and model-form uncertainty. The parameter uncertainty can be associated with the interface energy σ, latent heat L_H, solute diffusivity D_l, and local velocity of the interface V_I.

3.4 The effect of cooling rate

In order to investigate the effect of cooling rate on dendritic morphology and composition distribution, a higher cooling rate $\dot{T} = 4 \times 10^4$ K/s is used. The release of latent heat is included in this case. The simulation results are presented in FIGURE 5. It is observed that the growth velocity of dendrites increases with cooling rate. As a result, the secondary arms merge with each other and disappear. Besides, a higher cooling rate results in the generation of more nuclei. The melt is almost completely solidified at the time of 2.4 ms as shown in FIGURE 5(c). Because of the competitive growth of different grains, a small grain is merged with its neighbor grain, which is highlighted in a dashed rectangle, as shown in FIGURE 5. The final grain structure in FIGURE 5(d) is different from those in FIGURE 2(d) and FIGURE 3(d) because the increased cooling rate influences the competitive growth of dendrites. The rising cooling rate also increases the microsegregation at grain boundaries, as shown in FIGURE 5(e). FIGURE 5(f) shows that the temperature is lower than that in the case with the cooling rate $\dot{T} = 2 \times 10^4$ K/s in Section 3.3.

3.5 Quantitative analysis

In this section, a quantitative analysis is conducted to compare the effects of latent heat and cooling rate on temperature field, dendritic morphology, and composition field. FIGURE 6 shows the thermal histories at the location of $x = 50$ μm, $y = 25$ μm for different situations. When the release of latent heat is not considered, the temperature decreases linearly. When the release of latent heat is considered and the nominal cooling rate is $\dot{T} = 2 \times 10^4$ K/s, the temperature drops quasi-linearly at the beginning of solidification ($0 \leq t < 0.4$ ms). Since the fraction of phase transition is small at the beginning, the effect of latent heat is not obvious. When $t \geq 0.4$ ms, the temperature decreases slowly, then starts to increase at the time of 1.6 ms, and finally reaches a plateau because of the continuous release of latent heat. This phenomenon is widely known as recalescence during solidification of alloys. When the cooling rate is increased to $\dot{T} = 4 \times 10^4$ K/s, the effect of latent heat on the temperature field is reduced. The temperature decreases linearly at the beginning of solidification ($0 \leq t < 0.4$ ms), and then drops slowly with a decreasing cooling rate.

(a) Phase field at 0.8 ms

(b) Phase field at 1.6 ms

(c) Phase field at 2.4 ms

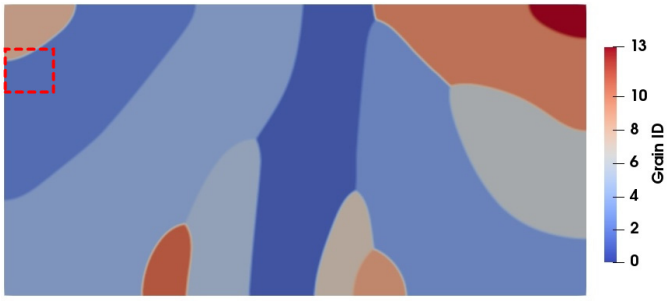

(d) Phase field at 3.2 ms

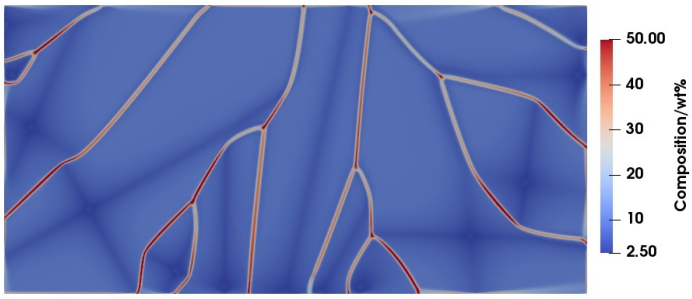

(e) Composition field at 3.2 ms

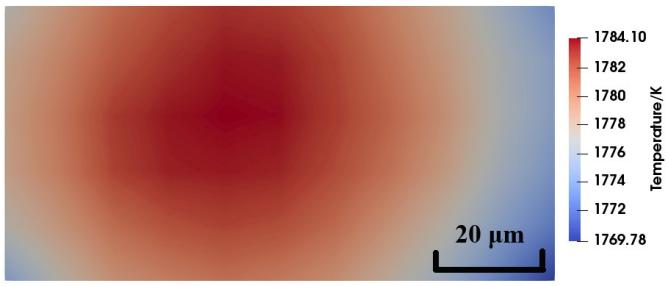

(f) Temperature field at 3.2 ms

FIGURE 5: Dendritic growth with latent heat when $\dot{T} = 4 \times 10^4$ K/s.

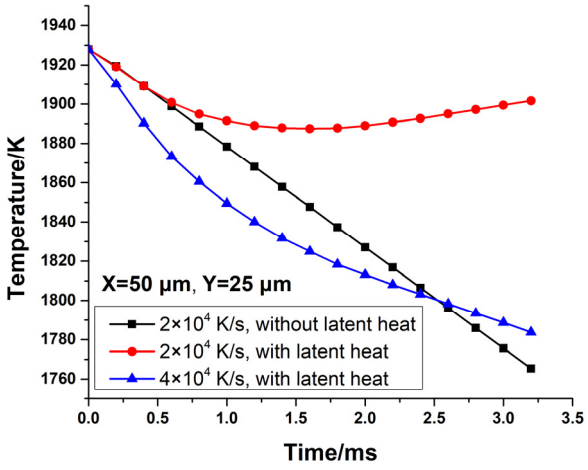

FIGURE 6: Thermal histories at the location of $x = 50$ μm, $y = 25$ μm under different conditions.

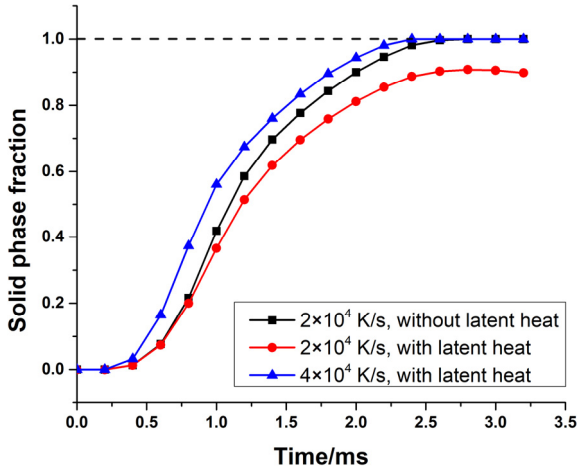

FIGURE 7: Time histories of solid phase fraction under different conditions.

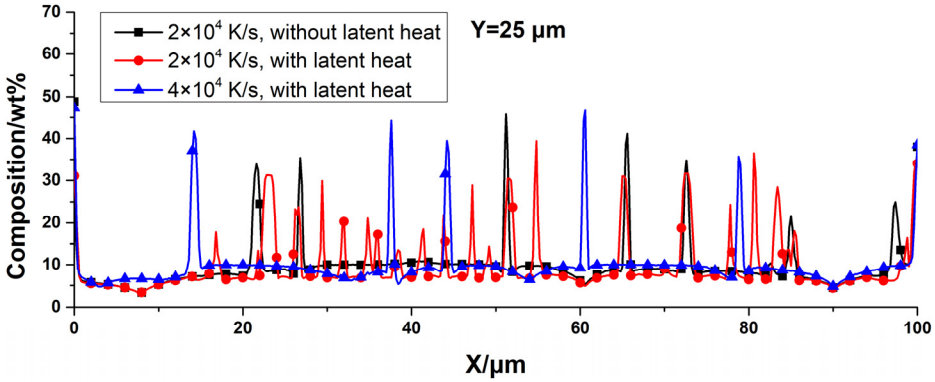

FIGURE 8: Composition distributions at the location of $y = 25$ μm at the time of 3.2 ms under different conditions.

The time histories of solid phase fraction for different cases are shown in FIGURE 7. Here, the solid phase fraction means the total fraction of solid phases in the simulation domain. When solid phase fraction equals to one, it means that the melt is completely solidified. The time histories of solid phase fraction look like "S"-shaped logistic sigmoid functions, which increase slowly at the beginning, then increase rapidly and reach plateaus in the end. When the latent heat is ignored, the solid phase fraction reaches 1.0 at the time of 2.8 ms, meaning that the liquid-solid phase transition is finished. When the latent heat is considered and the nominal cooling rate is $\dot{T} = 2 \times 10^4$ K/s, the solid phase fraction is 0.89 at the time of 2.4 ms, and then it reaches the plateaus. It will take some additional time to finish the solidification process because of the release of latent heat. When the cooling increases to $\dot{T} = 4 \times 10^4$ K/s, the speed of phase transition increases and the phase transition finishes at the time of 2.6 ms.

The composition distributions at the location of $y = 25$ μm at the time of 3.2 ms under different conditions are shown in FIGURE 8. It is observed that the locations where microsegregation occurs are mostly the same for different cases. The microsegregation can be defined as

$$\chi = \frac{C_{max}}{C_{min}}, \tag{30}$$

where C_{max} is the maximum of composition, and C_{min} is the minimum of composition. When the latent heat is ignored, the microsegregation is overestimated, which is $\chi = 48.87/3.23 = 15.13$. When the latent heat is considered and the nominal cooling rate is $\dot{T} = 2 \times 10^4$ K/s, there are more secondary arms and peaks of microsegregation. The microsegregation is $\chi = 39.44/3.23 = 12.21$. Therefore, the microsegregation without the latent heat is overestimated by at least 25% compared to that with the latent heat. When the cooling increases to $\dot{T} = 4 \times 10^4$ K/s, the microsegregation is $\chi = 47.30/4.73 = 10$.

Based on the above quantitative analysis, the inclusion of latent heat is important because it provides more realistic kinetics of dendritic growth and reduces overestimated microsegregation. The increased cooling rate increases the speed of phase transition and microsegregation.

4. CONCLUSION

In this work, a nucleation model is added into the previously developed PF-TLBM to consider the heterogeneous nucleation process at the solid-liquid interface. This mesoscale multi-physics model is used to simulate the nucleation and dendritic growth of Ti-6Al-4V alloy in the melt pool in SLM. A new method is proposed to estimate the thermal flux for a 2D small melt pool in order to approximate the actual non-isothermal temperature field in SLM. The simultaneous considerations of solute transport, heat transfer, nucleation, and dendritic growth are necessary to understand complex rapid solidification in SLM. By considering the release of latent heat, the model is able to predict the temperature field, composition distribution, and dendritic morphology with more detail than models without latent heat. The recalescence occurs when the latent heat is considered. The qualitative and quantitative analysis shows that the inclusion of latent heat is necessary because it reveals the details of the formation of secondary arms, reduces overestimated microsegregation and provides more realistic kinetics of dendritic growth. A higher cooling rate results in faster liquid-solid phase transition and higher microsegregation at grain boundaries.

Further work is needed to improve the fidelity, accuracy, and efficiency of the PF-TLBM model. For instance, the surface tension source term could be introduced into the TLBM so that the effect of Marangoni flow on dendritic growth can be investigated. The motion of grains can be enabled as well. Furthermore, the empirical nucleation parameters need to be determined by experimental observations, first-principles calculations, or atomistic simulations. The determination of nucleation energy barrier or nucleation rate can help to predict more realistic microstructure. The model-form and parameter uncertainties associated with the developed model should be quantified to provide more confidence of the prediction. A parallelized 3D PF-TLBM is needed to simulate the dendritic growth in the melt pool with much more details. Both the PFM

and the TLBM can be modified for parallel computation without much difficulty.

The proposed mesoscale multi-physics PF-TLBM model is a key component in a multiscale simulation framework for SLM processes, which involves multiple and complex physical phenomena. It predicts the microstructure evolution in the SLM process at a reasonable time scale. The predicted microstructure is the central hinge of the P-S-P relationship, which needs to be investigated for process design and optimization. Classical continuum simulation methods cannot provide fine-grained material phase and composition distribution, whereas atomistic models cannot simulate the time scales which are long enough for manufacturing processes.

ACKNOWLEDGEMENTS

This work is supported in part by the George W. Woodruff Faculty Fellowship at Georgia Institute of Technology.

REFERENCES

[1] Jaafar, M. A., Rousse, D. R., Gibout, S., and Bédécarrats, J. P., 2017, "A Review of Dendritic Growth during Solidification: Mathematical Modeling and Numerical Simulations," Renew. Sustain. Energy Rev., **74**(March), pp. 1064–1069.

[2] Steinbach, I., 2009, "Phase-Field Models in Materials Science," Model. Simul. Mater. Sci. Eng., **17**(7), p. 073001.

[3] Steinbach, I., 2013, "Why Solidification? Why Phase-Field?," Jom, **65**(9), pp. 1096–1102.

[4] Choudhury, A., Reuther, K., Wesner, E., August, A., Nestler, B., and Rettenmayr, M., 2012, "Comparison of Phase-Field and Cellular Automaton Models for Dendritic Solidification in Al-Cu Alloy," Comput. Mater. Sci., **55**, pp. 263–268.

[5] Keller, T., Lindwall, G., Ghosh, S., Ma, L., Lane, B. M., Zhang, F., Kattner, U. R., Lass, E. A., Heigel, J. C., Idell, Y., Williams, M. E., Allen, A. J., Guyer, J. E., and Levine, L. E., 2017, "Application of Finite Element, Phase-Field, and CALPHAD-Based Methods to Additive Manufacturing of Ni-Based Superalloys," Acta Mater., **139**, pp. 244–253.

[6] Wang, X., and Chou, K., 2019, "Microstructure Simulations of Inconel 718 during Selective Laser Melting Using a Phase Field Model," Int. J. Adv. Manuf. Technol., pp. 2147–2162.

[7] Acharya, R., Sharon, J. A., and Staroselsky, A., 2017, "Prediction of Microstructure in Laser Powder Bed Fusion Process," Acta Mater., **124**, pp. 360–371.

[8] Liu, D., and Wang, Y., 2017, "Mesoscale Multi-Physics Simulation of Solidification in Selective Laser Melting Process Using a Phase Field and Thermal Lattice Boltzmann Model," *Volume 1: 37th Computers and Information in Engineering Conference*, ASME, p. V001T02A027.

[9] Liu, D., and Wang, Y., 2019, "Mesoscale Multi-Physics Simulation of Rapid Solidification of Ti-6Al-4V Alloy," Addit. Manuf., **25**.

[10] SHIMONO, Y., Oba, M., NOMOTO, S., KOIZUMI, Y., and CHIBA, A., 2017, "Analysis of Solidification Microstructure in Additive Manufacturing by Multi-Phase Field Method," Proc. Comput. Mech. Conf., (August), p. 197.

[11] Gránásy, L., Börzsönyi, T., and Pusztai, T., 2002, "Crystal Nucleation and Growth in Binary Phase-Field Theory," J. Cryst. Growth, **237**–**239**(1–4), pp. 1813–1817.

[12] Gránásy, L., Börzsönyi, T., Börzsönyi, T., and Pusztai, T., 2002, "Nucleation and Bulk Crystallization in Binary Phase Field Theory," Phys. Rev. Lett., **88**(20), pp. 2061051–2061054.

[13] Gránásy, L., Pusztai, T., Saylor, D., and Warren, J. A., 2007, "Phase Field Theory of Heterogeneous Crystal Nucleation," Phys. Rev. Lett., **98**(3), pp. 1–4.

[14] Pusztai, T., Tegze, G., Tóth, G. I., Környei, Ĺ., Bansel, G., Fan, Z., and Gŕńsy, Ĺ., 2008, "Phase-Field Approach to Polycrystalline Solidification Including Heterogeneous and Homogeneous Nucleation," J. Phys. Condens. Matter, **20**(40).

[15] Simmons, J. P., Wen, Y., Shen, C., and Wang, Y. Z., 2004, "Microstructural Development Involving Nucleation and Growth Phenomena Simulated with the Phase Field Method," Mater. Sci. Eng. A, **365**(1–2), pp. 136–143.

[16] Li, J., Wang, J., and Yang, G., 2007, "Phase-Field Simulation of Microstructure Development Involving Nucleation and Crystallographic Orientations in Alloy Solidification," J. Cryst. Growth, **309**(1), pp. 65–69.

[17] Aziz, M. J., 1982, "Model for Solute Redistribution during Rapid Solidification," J. Appl. Phys., **53**(2), pp. 1158–1168.

[18] Antonysamy, A. A. A., 2012, "Microstructure , Texture and Mechanical Property Evolution during Additive Manufacture of Ti6Al4V Alloy Using Laser , Electron Beam , and Arc Melting Techniques for Aerospace Applications School of Materials," (Doctoral Diss. Univ. Manchester (United Kingdom)), pp. 1–272.

[19] 2019, "OpenPhase" [Online]. Available: http://www.openphase.de/.

[20] Antonysamy, A. A., Meyer, J., and Prangnell, P. B., 2013, "Effect of Build Geometry on the β-Grain Structure and Texture in Additive Manufacture of Ti6Al4V by Selective Electron Beam Melting," Mater. Charact., **84**, pp. 153–168.

[21] Thijs, L., Kempen, K., Kruth, J. P., and Van Humbeeck, J., 2013, "Fine-Structured Aluminium Products with Controllable Texture by Selective Laser Melting of Pre-Alloyed AlSi10Mg Powder," Acta Mater., **61**(5), pp. 1809–1819.

[22] Bouchard, D., and Kirkaldy, J. S., 1996, "Equations and Specification of Predictive Procedures," Metall. Mater. Trans. B, **28B**(4), pp. 651–663.

